
Multiple antiferromagnetic phases and magnetic anisotropy in exfoliated CrBr₃ multilayers

Fengrui Yao^{1,2}, Volodymyr Multian^{1,2,3}, Zhe Wang⁴, Nicolas Ubrig^{1,2}, Jérémie Teyssier^{1,2}, Fan Wu^{1,2}, Enrico Giannini¹, Marco Gibertini^{5,6}, Ignacio Gutiérrez-Lezama^{1,2} and Alberto F. Morpurgo^{1,2*}

¹*Department of Quantum Matter Physics, University of Geneva, 24 Quai Ernest Ansermet, CH-1211 Geneva, Switzerland*

²*Department of Applied Physics, University of Geneva, 24 Quai Ernest Ansermet, CH-1211 Geneva, Switzerland*

³*Advanced Materials Nonlinear Optical Diagnostics lab, Institute of Physics, NAS of Ukraine, 46 Nauky pr., 03028 Kyiv, Ukraine*

⁴*MOE Key Laboratory for Nonequilibrium Synthesis and Modulation of Condensed Matter, Shaanxi Province Key Laboratory of Advanced Materials and Mesoscopic Physics, School of Physics, Xi'an Jiaotong University, Xi'an, 710049, China*

⁵*Dipartimento di Scienze Fisiche, Informatiche e Matematiche, University of Modena and Reggio Emilia, IT-41125, Modena, Italy*

⁶*Centro S3, CNR-Istituto Nanoscienze, IT-41125, Modena, Italy*

*Correspondence: alberto.morpurgo@unige.ch

ABSTRACT

In twisted two-dimensional (2D) magnets, the stacking dependence of the magnetic exchange interaction can lead to regions of ferromagnetic and antiferromagnetic interlayer order, separated by non-collinear, skyrmion-like spin textures. Recent experimental searches for these textures have focused on CrI_3 , known to exhibit either ferromagnetic or antiferromagnetic interlayer order, depending on layer stacking. However, the very strong uniaxial anisotropy of CrI_3 disfavors smooth non-collinear phases in twisted bilayers. Here, we report the experimental observation of three distinct magnetic phases –one ferromagnetic and two antiferromagnetic– in exfoliated CrBr_3 multilayers, and reveal that the uniaxial anisotropy is significantly smaller than in CrI_3 . These results are obtained by magnetoconductance measurements on CrBr_3 tunnel barriers and Raman spectroscopy, in conjunction with density functional theory calculations, which enable us to identify the stackings responsible for the different interlayer magnetic couplings. The detection of all locally stable magnetic states predicted to exist in CrBr_3 and the excellent agreement found between theory and experiments, provide complete information on the stacking-dependent interlayer exchange energy and establish twisted bilayer CrBr_3 as an ideal system to deterministically create non-collinear magnetic phases.

The emergence of smooth non-collinear magnetic phases in twisted bilayers of two-dimensional (2D) magnetic semiconductors relies on the different roles of intra and interlayer exchange interaction, and depends crucially on the strength of uniaxial magnetic anisotropy¹⁻⁶. Since 2D magnetic semiconductors are formed by covalently bonded layers held together by weak van der Waals forces⁷⁻¹², the intralayer exchange is relatively strong and drives long-range magnetic ordering if magnetic anisotropy is also strong enough. Interlayer exchange is much weaker but has a key role, especially in 2D magnets whose spins point in the same direction within each layer, because it determines whether the system is a ferromagnet or a layered antiferromagnet¹³⁻¹⁹. As the strength and sign of interlayer exchange vary rapidly with atomic distances, whether interlayer coupling is ferromagnetic (FM) or antiferromagnetic (AFM) depends critically on layer stacking²⁰⁻²⁶. It follows that in layers twisted with a small relative angle, the resulting moiré pattern causes the interlayer coupling to vary periodically in space and creates a lattice of relatively large islands, whose magnetic order is determined by the corresponding local atomic stacking. Non-collinear magnetic phases emerge when the moiré periodicity induces alternating FM and AFM islands, and the uniaxial anisotropy –while being sufficiently strong to stabilize long-range order within one layer– is not so strong to prevent smooth canting of the spins in the regions between the islands¹⁻⁶.

The Chromium trihalides (CrX_3 ; $X = \text{I, Br, Cl}$)²⁷⁻⁴⁰, with ferromagnetically aligned spin within individual layers and stacking-dependent interlayer exchange interaction, offer ideal conditions to search for non-collinear moiré magnetic phases. That is why recent pioneering experiments have focused on twisted bilayer CrI_3 ^{41, 42}. However, since Iodine has the largest atomic number and therefore the strongest spin-orbit interaction⁴³, the very large uniaxial anisotropy of CrI_3 makes twisted bilayer of this compound not optimal for the stabilization of non-collinear phases. In the opposite limit, in CrCl_3 , spin-orbit interaction is weak and experiments have established that the magnetic anisotropy is correspondingly weak, causing the ferromagnetic transition in monolayers to be of the Kosterlitz-Thouless type, without truly long-range order⁴⁴. It should therefore be hoped that CrBr_3 may be suitable to engineer non-collinear magnetic phases in twisted bilayers, because its uniaxial anisotropy –while being sufficiently large to ensure ferromagnetic long-range order in

monolayers³⁸ is expected to be much weaker than in CrI₃. So far, however, this remains unexplored experimentally and, moreover, further progress is hampered because only FM coupling has been reported in exfoliated CrBr₃ multilayers^{32, 38-40}. To exploit the potential of CrBr₃ for the search of non-collinear magnetic phases in twisted bilayers it is therefore essential to demonstrate structures with both FM and AFM interlayer coupling in exfoliated layers, to fully characterize their interlayer magnetic exchange interaction, and to establish that the strength of magnetic anisotropy is indeed sizably smaller than in CrI₃.

Here, we report the observation of exfoliated CrBr₃ multilayers with three distinct magnetic interlayer couplings –and correspondingly distinct magnetic orders– which we associate to different stackings of the constituent CrBr₃ monolayers. We detect these different magnetic states by performing magnetoconductance measurements on tunnel junctions realized with exfoliated CrBr₃ multilayers that are found to include parts with different layer stackings, resulting in different interlayer exchange couplings. In particular, we find that –besides the FM interlayer coupling responsible for bulk ferromagnetism– two distinct AFM states are present. One of these AFM states appears to be the same observed in films grown by molecular beam epitaxy⁴⁵ and the other had not been observed earlier. Multilayers exhibiting different magnetic states are fingerprinted by the splitting of specific Raman modes, which enables us to establish the symmetry of the layer stackings corresponding to the different magnetic phases. Magnetoconductance measurements performed on the AFM multilayers also enable us to determine the magnetic anisotropy of CrBr₃ –approximately four times weaker than in CrI₃– and the full phase diagram. We find that the critical temperatures of all stacking-dependent magnetic phases are very close, as expected for 2D magnets in which the interlayer coupling is much weaker than the intralayer one. Our experimental results are in full agreement with the density functional theory calculations of Ref.²⁴ (whose basic aspects are summarized in Fig. 1), and represent the first observation of all predicted magnetic states of CrX₃ multilayers (in all CrX₃ only two of the three predicted locally stable configurations had been reported experimentally). These results provide all the needed information to engineer and analyze the magnetic phases of twisted bilayer CrBr₃.

To illustrate how tunneling magnetoconductance measurements are employed to determine the interlayer magnetic coupling (or the magnetic state) of thin 2D magnetic semiconductors, we start by discussing the known magnetoconductance of devices realized on multilayers of either FM CrBr₃^{32-39, 40} or layered AFM CrI₃²⁸⁻³¹ (see Fig. 2a for the device schematics). Electron transport in these devices is phenomenologically understood in terms of Fowler-Norheim (FN) tunneling^{28-31, 40}, with the electric field generated by the applied bias that tilts the conduction band in the barrier, causing an exponential increase in tunneling probability (Fig. 2b). The process results in strongly non-linear I - V curves (Fig. 2c), such that $\ln(I/V^2)$ is proportional to $1/V$ (Fig. 2d). A finite magnetoconductance ($\delta G(H, T) = (G(H, T) - G_0(T))/G_0(T)$, where $G(H, T)$ is the conductance measured at magnetic field H and temperature T and $G_0(T) = G(H = 0, T)$) occurs because the magnetic state of the material determines the height of the tunnel barrier^{28-31, 40}. The magnetoconductance, therefore, exhibits a characteristic evolution with H and T that is different for FM and layered AFM barriers.

For a FM barrier, the magnetoconductance is small at low T (Fig. 2e), because the spins are already nearly fully polarized for $H = 0$, and the magnetic state remains virtually unchanged when a finite H is applied⁴⁰. Characteristic “lobes” in the magnetoconductance appear in the critical region for $T \sim T_C$, due to the divergence of the magnetic susceptibility near the Curie temperature (Fig. 2f), such that the application of an even small magnetic field causes large changes in magnetization⁴⁰. In a strongly anisotropic layered antiferromagnet (Fig. 2g, h), instead, the magnetoconductance is large at low temperatures and exhibits two characteristic sharp jumps at a material-dependent field and twice that value (0.9 T and 1.8 T in CrI₃²⁸⁻³¹). The jumps originate from flipping the magnetization of the outer layers in the barrier (at 0.9 T) and of the inner ones (at 1.8 T), with the value of 0.9 T providing a direct measure of the strength of interlayer exchange. Importantly, the sequence of jumps differs for bi-, tri- and thicker layers: bi- and tri-layer show only one jump at 0.9 T or 1.8 T, respectively; four or thicker layers show two jumps at 0.9 T and 1.8 T²⁸⁻³¹. Therefore, magnetoconductance measurements on magnetic tunnel barriers indicate unambiguously whether the interlayer coupling is FM or AFM, and for antiferromagnets, provide information about the number of layers.

One of our key experimental observations comes from magnetoconductance measurements on CrBr₃ tunnel barriers realized with multilayers exfoliated from crystals in which Raman spectra show an additional peak of sizable magnitude (at approximately 161 cm⁻¹; see Supplementary Fig. 1 for detail), which we attribute to the presence of an allotrope of CrBr₃ different from the known thermodynamically stable structure (due to a different stacking of the CrBr₃ layers^{46,47}). Specifically, the data shown in Fig. 2e,f –with small and featureless magnetoconductance at low T – are characteristic of CrBr₃ tunnel barriers realized with thin multilayers with layers fully stacked as in the FM state of the material (as discussed in our earlier work⁴⁰). In several other tunnel barriers, however, the magnetoconductance is different, as illustrated by five representative devices in Fig. 3a: it is much larger and exhibits sharp jumps. The jumps occur at a few different specific values of magnetic field (as indicated by the vertical grey dashed lines) for all the measured samples. The analysis of these jumps provides clear information about the different types of naturally occurring interlayer couplings between adjacent CrBr₃ layers, depending on their stacking.

We observed jumps in the magnetoconductance of 12 (out of 20) different CrBr₃ samples, with thicknesses ranging from 2.8 nm to 20 nm (Supplementary Fig. 2). Fig. 3b summarizes the magnetic field values at which the jumps occur: 0.55 T and twice this value (1.1 T), and 0.2 T and twice this value (0.4 T). Finding jumps reproducibly occurring at the same values of H and twice those values is a clear manifestation of spin-flip transitions, typical of AFM coupled layers with uniaxial magnetic anisotropy. The fact that two different field values are observed (0.2 T and 0.55 T) indicates the occurrence of two distinct types of AFM couplings in CrBr₃ devices. With reference to the magnitude of the field, we abbreviate them as L-type (“large”) and S-type (“small”) AFM coupling. The histogram in Fig. 3c gives clear statistical indications as to the occurrence of L and S jumps. S-type jumps at 0.2 T occur with nearly the same frequency as L-type jumps at 0.55 T. However, the number of jumps with “twice” the field (i.e., jumps at 0.4 T and 1.1 T) differs in the two cases. Only two out of seven devices that show a jump at 0.2 T also show a jump at 0.4 T, indicating that most commonly, only two layers are stacked in the way giving S-type coupling, and that longer sequences occur more

rarely. On the contrary, most of the devices (6 out of 8) exhibiting a jump at 0.55 T also exhibit a jump at 1.1 T, indicating that for the stacking leading to L-type magnetoconductance jumps, sequences of four or more layers can be found relatively easily. These observations indicate that long sequences of CrBr₃ layers stacked in the way needed to produce S-type jumps are energetically more costly than for the other types of stacking (the stacking producing L-type magnetoconductance jumps and those giving rise to ferromagnetism), which is why they occur more rarely.

We attribute the occurrence of two distinct AFM phases to the presence in the tunnel barriers of layer sequences with two different layer stacking, resulting in different interlayer exchange couplings. To confirm the occurrence of different stackings in CrBr₃ devices with FM interlayer coupling, or L/S-type AFM interlayer coupling, we performed Raman spectroscopy at 10 K (Fig. 3d and Supplementary Fig. 3). Measurements with either parallel (XX configuration) or perpendicular (XY configuration) polarization of the incident and detected light were done, focusing on the modes in the 130 cm⁻¹ - 170 cm⁻¹ range^{48, 49}, predicted to be particularly sensitive to the stacking (details are provided in the method section). To allow a direct comparison, the Raman data shown have been measured in all cases on four-layer tunnel barriers. The Raman spectra of a CrBr₃ FM device (magnetoconductance data shown in Fig. 2e and Fig. 2f) show two peaks at ~142 cm⁻¹ and 152 cm⁻¹ that can be assigned to two twofold degenerate E_g modes, whose position and intensity are independent of the polarization alignment (top panel, Fig. 3d). This is consistent with AB stacked CrBr₃, as already discussed in the literature^{48, 49}. In contrast, the sample in which L-type switching is observed (see Sample 8 in Supplementary Fig. 2 for detail) exhibits two additional peaks (~146 cm⁻¹ and 160 cm⁻¹) when measured in the XX configuration, whose relative intensity changes in the XY configuration (middle panel, Fig. 3d). This behavior is indicative of layers with monoclinic (M) stacking (see Fig. 1b), whose broken rotational symmetry results in the splitting of the two twofold degenerate E_g modes⁵⁰⁻⁵³. Finally, for the sample exhibiting S-type switching (see Sample 10 in Supplementary Fig. 2 for detail), again only two peaks are observed at positions close to (but not identical) to those of FM CrBr₃, independently of the polarization configuration employed, which is expected for AA stacking (see Fig. 1b) with three-fold rotational symmetry.

The magnetotransport measurements and the observed Raman spectra are fully consistent with the density functional theory (DFT) calculations in Ref.²⁴, which predict three local minima in the total energy of CrBr₃, corresponding to distinct stacking configurations, with the interlayer coupling that is FM for one and AFM for the other two (Fig.1; the number of locally stable configurations is three also in other DFT studies^{3, 25}, but the sign of the interlayer exchange differs, depending on details of the calculations). According to Ref. ²⁴, one of the two AFM stackings (AA, Fig. 1b) has a high symmetry (and should therefore give only two degenerate E_g modes) and has a total energy that is sizably larger than the other two stacking (which is why long sequences of layers are found less frequently). Therefore, we attribute S-type magnetoconductance jumps (at 0.2 T and 0.4 T) to AA stacking, and the L-type jumps (at 0.55 T and 1.1 T) to monoclinic stacking. This attribution is consistent with the observed Raman spectra, because the monoclinic stacking has relatively lower symmetry (see Fig.1b) and gives rise to additional Raman peaks resulting from the splitting of the degenerate E_g mode⁵⁰⁻⁵³. Note that the L-type jumps perfectly match the critical field previously observed in CrBr₃ bilayers synthesized by molecular beam epitaxy⁴⁵, although our analysis -in particular the Raman data- attributes it to a different configuration with respect to that suggested in Ref.⁴⁵. We conclude that the DFT calculations in Ref.²⁴ capture all key aspects of the relation between structure and magnetism in CrBr₃ multilayers.

We emphasize that –despite the very systematic behavior of the jumps in magnetoconductance that only occur at four selected values of magnetic field, as expected for two distinct types of AFM multilayers– our observations pose some questions as to how regions exhibiting different magnetic orders are magnetically coupled to each other. If the regions are coupled either ferromagnetically or antiferromagnetically through one of the three stacking identified here above, a simple analysis of the magnetic energy of multilayers containing multiple types of stacking indicates that magnetoconductance jumps should be expected to occur at many different magnetic fields determined by the precise stacking sequence of the entire multilayer, and not only at the fields observed in the experiments. Finding that jumps are only visible at the values expected for isolated multilayers of the

different magnetic states seems to be only compatible with a scenario in which sequences with different stacking in a same multilayer are magnetically decoupled, so that they can re-orient independently when a magnetic field is applied. The decoupling probably originates from the presence of large misorientation (i.e., large twist angles) between layers that separate distinct stacking configurations, which occur spontaneously during the crystal growth process (i.e., whenever it occurs during the growth, such a misorientation between adjacent layers makes it energetically more favorable for the stacking sequence to change).

To further support the scenario outlined here above, we sought to realize tunnel barriers based on an isolated AFM multilayer, which allow us to test experimentally if indeed the magnetoconductance jumps are observed at the expected values in a device realized with a fully well-defined AFM structure. Given the relatively high probability to find long sequences of layers (4L or thicker) with L-type stacking, we did succeed in realizing a perfectly L-type stacked 4L tunnel barrier device (see also Supplementary Fig. 4) and in measuring its T - and H - dependent transport properties systematically. Fig. 4a-c compares the low-temperature ($T = 2$ K) magnetotransport measurements performed on this L-type 4L barrier (green curves) with data measured on a “conventional” FM CrBr₃ 4L tunnel barrier (orange curves). The 4L L-type barrier behaves precisely as anticipated, exhibiting magnetoconductance jumps at 0.55 T and 1.1 T (i.e., the values identified above). The difference between the magnetoconductance of the AFM and FM barriers is obvious, irrespective of whether the magnetic field is applied perpendicular (Fig. 4a) or parallel (Fig. 4b) to the plane. For devices of the same thickness, the low temperature ($T = 2$ K) magnetoconductance is more than ten times larger for the AFM L-type device. When the field is applied in-plane, measurements show that the magnetoconductance exhibits no jumps and extends to a higher magnetic field (nearly 2 T), a consequence of the magnetic anisotropy in CrBr₃. Importantly, this observation indicates that the magnetic anisotropy in CrBr₃ is much smaller than in CrI₃, where the in-plane magnetoconductance extends up to 6 T³⁰, more than three times larger than in CrBr₃. Through a simple analysis that considers the joint effect of anisotropy and interlayer exchange, this difference implies that the magnitude of the uniaxial anisotropy in CrBr₃ is more than four times smaller than in CrI₃. Also, the

temperature dependence of the tunneling conductance (Fig. 4c) is different for the FM and the L-type AFM barriers: in the FM barrier, the conductance increases when T is lowered below T_C (~ 31 K, smaller than that of thick layers) whereas for the AFM L-type barrier, a steeper decrease in conductance occurs below Néel temperatures T_N^L (~ 29 K), again, similar trend as in CrI_3 ³⁰. In short, the differences between L-type CrBr_3 and CrI_3 barriers are exclusively of quantitative nature, with CrI_3 exhibiting larger interlayer exchange, magnetic anisotropy, and magnetoconductance, trends that are all captured by the DFT-based calculations²⁴.

Full measurements of the conductance as a function of T and H are shown in Fig. 5, and exhibit all trends expected for a layered antiferromagnet. Whereas for $H = 0$ T, the tunneling conductance decreases below T_N upon cooling, it increases when a sufficiently large magnetic field (~ 1 T) is applied (Fig. 5a). Additionally, as T is increased, the magnetoconductance becomes smaller and the jumps shift to lower magnetic field (Fig. 5b). The color plot of the magnetoconductance as a function of T and H in Fig. 5c –which represents the magnetic phase diagram of the L-type 4L barrier– summarizes the results, and shows the phase boundaries separating the different magnetic states: the AFM phase at low field (I), the intermediate regime with the magnetization of the outer layers flipped (II) and the spin-flip phase at high field (III).

Having access to tunnel barriers made of different allotropes of CrBr_3 , with different magnetic states, enables their critical temperatures to be compared. That is why –after determining T_C for the FM structure and T_N for the L-type AFM state– we measured the temperature and magnetic field dependence of the tunneling conductance in a barrier showing S-type magnetoconductance jumps. Because long sequences of S-type stacking are rare, we could only measure a tunnel barrier with S-stacked bilayers close to one of the contacts and the remaining layers stacked in the structure producing ferromagnetism (see Supplementary Fig. 5). The T - and H -dependence of the magnetoconductance (Fig. 5d) then exhibits concomitantly signatures of S-type antiferromagnetism (visible jump at 0.2 T at sufficiently low temperature) and of the FM state of CrBr_3 (the “lobes” of enhanced magnetoconductance near the Curie temperature at 32-34 K⁴⁰). Although the concomitance

of these different features makes a precise determination of the Néel temperature less straightforward, we find that the magnetoconductance jumps disappear at ~ 28 K (Fig. 5e). The Curie temperature of the FM state of CrBr_3 and the Néel temperatures of the L-type and S-type AFM states are therefore 31 K, 29 K and 28 K, values that agree with theory in multiple regards (we summarize the properties of the three magnetic states in Table 1). Specifically, the critical temperature values are all very close, because the critical temperature of weakly coupled 2D magnetic layers is primarily determined by intralayer interactions and depends only weakly on the interlayer interaction (irrespective of whether the interlayer coupling is FM or AFM). Indeed, the correction to the critical temperature of an isolated monolayer is predicted to scale with $|J_L/J|$ (J_L and J are the inter- and intra-layer exchange couplings)^{54, 55}, a scaling consistent with our finding that S-type stacking, which exhibits a lower T_N than L-type stacking, also exhibits a lower J_L (as inferred from the smaller magnetic field at which the magneto conductance jumps occur). Additionally, the Curie temperature of FM CrBr_3 is larger than Néel temperatures of both AFM states, in perfect agreement with DFT calculations that predict a sizably larger value of J_L in the FM state than $|J_L|$ in the AA and M stacking configurations^{24, 25} (see Fig. 1b).

Even though more direct experimental observations relating the different stackings of CrBr_3 multilayer tunnel barriers to their magnetoconductance properties would be desirable (e.g., by directly observing the layer stacking in the barriers used for transport measurements), our results provide a rather complete, and fully consistent characterization of stacking-dependent magnetism in CrBr_3 multilayers. Continuum models of small-angle and long-period moiré bilayers take the twist angle, the local strength of the interlayer exchange coupling as a function of layer registry, and the magnetic anisotropy as input, to calculate the expected magnetic state. For CrI_3 layers used to search for non-collinear magnetic phases in twisted bilayers, such a wealth of information is not available. For instance, the local strength of the interlayer exchange interaction as a function of relative shift between the layer is not known experimentally, and only two of the three expected magnetic states have been observed in experiments^{29, 56}. Additionally, the large uniaxial magnetic anisotropy of CrI_3 reduces the portion of the phase diagram where the non-collinear phase can emerge, which imposes

more stringent conditions on the twist angle. The work presented here clearly shows that the situation for CrBr₃ is different. Both the experimental observation of all three predicted locally stable magnetic states, and the overall agreement found with the calculations indicate that our understanding of interlayer exchange as a function of layer registry is in fact rather detailed and complete. The magnetic anisotropy of CrBr₃, being more than four times smaller than in CrI₃, is ideal and increases the parameter regime in which non-collinear magnetic phases can be found. We therefore conclude that CrBr₃ offers the most favorable conditions among all Chromium trihalides to controllably engineer and model non-collinear magnetic states in twisted bilayer structures.

Acknowledgments

The authors gratefully acknowledge Alexandre Ferreira for technical support. A. F. M. gratefully acknowledges the Swiss National Science Foundation and the EU Graphene Flagship project for support. M.G. acknowledges support from the Italian Ministry for University and Research through the Levi-Montalcini program. Z.W. acknowledges support from National Natural Science Foundation of China (11904276) and the Fundamental Research Funds for the Central Universities.

Data availability

All relevant data are available from the corresponding authors upon reasonable request.

Code availability

All codes adopted for DFT calculation are open source and available at <https://gitlab.com/QEF/q-e>.

Author contributions

F.Y. and Z.W. fabricated the devices and performed the transport measurements with the help of I.G.L. A.F.M. initiated and supervised the project. V.D. and F.Y. performed optical measurements with help of N.U. and J.T.; E.G. and F.W. grew the crystals. M.G. performed ab-initio calculations. A.F.M., M.G., I.G.L. and F.Y. analyzed the data and wrote the manuscript with input from all authors. All authors discussed the results.

Competing financial interests: The authors declare no competing financial interests.

METHODS

DFT calculation

First-principles simulations are performed within density-functional theory (DFT) using the Quantum ESPRESSO distribution^{57, 58}. To account for van der Waals interactions between the layers, the spin-polarised extension⁵⁹ of the revised vdW-DF2 exchange-correlation functional^{60, 61} is adopted, truncating spurious interactions between artificial periodic replicas along the vertical direction⁶²⁻⁶⁴. The Brillouin zone is sampled with a $8 \times 8 \times 1$ Γ -centered Monkhorst-Pack grid. Pseudopotentials are taken from the Standard Solid-State Pseudopotential (SSSP) accuracy library (v1.0)⁶⁵⁻⁶⁷ with increased cutoffs of 60 Ry and 480 Ry for wave functions and density, respectively. Total energy calculations as a function of the relative displacement between the layers are performed without atomic relaxations, by taking the structure of DFT-relaxed monolayers with the experimental lattice parameter and interlayer separation. For line scans, atomic positions are relaxed by reducing the force acting on atoms below a threshold of 26 meV/Å, while keeping fixed the in-plane coordinates of Cr atoms. All calculations are managed and automated using the AiiDA materials informatics infrastructure^{68, 69}.

Bulk crystal growth

CrBr₃ bulk crystals were grown by the chemical vapor transport method⁷⁰. The elemental precursors Chromium (99.95% CERAC) and TeBr₄ (99.9% Alfa Aesar) were mixed with a molar ratio 1:0.75 to a total mass of 0.5 g, and were placed in a quartz tube with a length of 13 cm to achieve a temperature gradient of approximately 10°C/cm from the hot end at 700°C to the cold end at 580°C. After seven days at this temperature, the furnace was switched off. When the tube cooled to room temperature, CrBr₃ crystals were found to crystallize towards the cold end of the tube, over a length that corresponded to a growth temperature range of ~ 650°C – 580°C. As shown in Supplementary Fig. 1, Raman spectroscopy measurements show that different crystals harvested from a same batch can exhibit the coexistence of at least two different structures.

Device fabrication

CrX₃ multilayers were first mechanically exfoliated from the bulk crystals, and tunnel junctions of multilayer HBN/graphene/CrX₃/graphene/HBN were assembled using a pick-and-lift technique⁷¹ with stamps of PDMS/PC in a glove box filled with nitrogen gas. The thickness of CrX₃ multilayers was obtained by atomic force microscope measurements performed on the encapsulated devices. Edge contacts to the graphene multilayers were made by electron beam lithography, reactive-ion etching, electron-beam evaporation (10 nm Cr /50 nm Ar), and lift-off process. Transport measurements were performed in a homemade low-noise electronics system combined with a helium cryostat from Oxford Instruments.

Raman measurement

All Raman spectroscopy measurements were performed using a Horiba system (Labram HR evolution) combined with a helium flow cryostat. The laser (532 nm, ~ 1 μ m) was linearly polarized with its polarization angle controlled via a half-wave plate (Thorlabs) and was focused on the sample (inside the cryostat) through a 50 X Olympus objective. The scattering light of the sample was collected by the same objective and passed through the analyzer, then was sent to a Czerni–Turner spectrometer equipped with a 1800 grooves mm⁻¹ grating and was detected by a liquid nitrogen-cooled CCD-array. Measurements under either parallel (XX) or crossed (XY) polarization were performed by varying the half-wave plate while keeping the analyzer on the detecting light path fixed. Similarly to previous reports⁵⁰⁻⁵³, the Raman tensors of doubly degenerate E_{g1} and E_{g2} modes (in the AB and AA stacking, $R\bar{3}$ group) and the non-degenerate A_g and B_g modes (in the monoclinic stacking, C2/m group) can be derived as:

$$E_{g1} = \begin{pmatrix} m & n & p \\ n & -m & q \\ p & q & 0 \end{pmatrix}, E_{g2} = \begin{pmatrix} n & -m & -q \\ -m & -n & p \\ -q & p & 0 \end{pmatrix}, A_g = \begin{pmatrix} a & 0 & d \\ 0 & c & 0 \\ d & 0 & b \end{pmatrix}, B_g = \begin{pmatrix} 0 & e & 0 \\ e & 0 & f \\ 0 & f & 0 \end{pmatrix}$$

As a result, for AB and AA stacked multilayers, the Raman intensity for the E_{g1} and E_{g2} modes as a function of θ can be derived as: $I_{(E_{g1})} \propto |m\sin(\theta) - n\cos(\theta)|^2$ and $I_{(E_{g2})} \propto |m\cos(2\theta) + n\sin(2\theta)|^2$, where θ is the polarized direction of excitation light with respect to the analyzer. Thus, the dependence on the polarization angle cancels out when the two modes (E_{g1} and E_{g2}) are degenerate, leading to one single E_g peak (the total intensity of the degenerate modes is the same under either XX configuration

or XY configuration; observed in Fig.3d, top panel and bottom panel). However, for the monoclinic stacking, the degenerate E_g modes split into the non-degenerate A_g and B_g modes. Since the B_g mode is distinct from the E_g mode and its Raman intensity as a function of θ can be expressed as: $I_{(B_g)} \propto e^2 \cos^2(\theta)$, different intensities of the Raman peaks under the XX configuration and XY configuration are observed (Fig.3d, middle panel).

REFERENCE

- 1 Tong, Q., Liu, F., Xiao, J., Yao, W. Skyrmions in the Moiré of van der Waals 2D Magnets. *Nano Lett* **18**, 7194-7199 (2018).
- 2 Hejazi, K., Luo, Z.-X., Balents, L. Noncollinear phases in moiré magnets. *PNAS* **117**, 10721-10726 (2020).
- 3 Xiao, F., Chen, K., Tong, Q. Magnetization textures in twisted bilayer CrX₃ (X= Br, I). *Phys Rev Res* **3**, 013027 (2021).
- 4 Akram, M., Erten, O. Skyrmions in twisted van der Waals magnets. *Phys Rev B* **103**, L140406 (2021).
- 5 Akram, M. et al. Moiré skyrmions and chiral magnetic phases in twisted CrX₃ (X= I, Br, and Cl) bilayers. *Nano Lett* **21**, 6633-6639 (2021).
- 6 Fumega, A. O., Lado, J. L. Moiré-driven multiferroic order in twisted CrCl₃, CrBr₃ and CrI₃ bilayers. *2D Materials* **10**, 025026 (2023).
- 7 Burch, K. S., Mandrus, D., Park, J. G. Magnetism in two-dimensional van der Waals materials. *Nature* **563**, 47-52 (2018).
- 8 Gong, C., Zhang, X. Two-dimensional magnetic crystals and emergent heterostructure devices. *Science* **363**, eaav4450 (2019).
- 9 Gibertini, M., Koperski, M., Morpurgo, A. F., Novoselov, K. S. Magnetic 2D materials and heterostructures. *Nat Nanotechnol* **14**, 408-419 (2019).
- 10 Mak, K. F., Shan, J., Ralph, D. C. Probing and controlling magnetic states in 2D layered magnetic materials. *Nat Rev Phys* **1**, 646-661 (2019).
- 11 Huang, B. et al. Emergent phenomena and proximity effects in two-dimensional magnets and heterostructures. *Nat Mater* **19**, 1276-1289 (2020).
- 12 Kurebayashi, H. et al. Magnetism, symmetry and spin transport in van der Waals layered systems. *Nat Rev Phys* **4**, 150-166 (2022).
- 13 Gong, C. et al. Discovery of intrinsic ferromagnetism in two-dimensional van der Waals crystals. *Nature* **546**, 265-269 (2017).
- 14 Huang, B. et al. Layer-dependent ferromagnetism in a van der Waals crystal down to the monolayer limit. *Nature* **546**, 270-273 (2017).
- 15 McGuire, M. A. Crystal and magnetic structures in layered, transition metal dihalides and trihalides. *Crystals* **7**, 121 (2017).
- 16 Otrokov, M. M. et al. Prediction and observation of an antiferromagnetic topological insulator. *Nature* **576**,

416-422 (2019).

- 17 Kong, T. et al. VI_3 —a new layered ferromagnetic semiconductor. *Adv Mater* **31**, 1808074 (2019).
- 18 Telford, E. J. et al. Layered antiferromagnetism induces large negative magnetoresistance in the van der Waals semiconductor CrSBr . *Adv Mater* **32**, e2003240 (2020).
- 19 Bud'ko, S. L., Gati, E., Slade, T. J., Canfield, P. C. Magnetic order in the van der Waals antiferromagnet CrPS_4 : Anisotropic H–T phase diagrams and effects of pressure. *Phys Rev B* **103**, 224407 (2021).
- 20 Sivadas, N. et al. Stacking-dependent magnetism in bilayer CrI_3 . *Nano Lett* **18**, 7658-7664 (2018).
- 21 Jiang, P. H. et al. Stacking tunable interlayer magnetism in bilayer CrI_3 . *Phys Rev B* **99**, 144401 (2019).
- 22 Soriano, D., Cardoso, C., Fernández-Rossier, J. Interplay between interlayer exchange and stacking in CrI_3 bilayers. *Solid State Commun* **299**, 113662 (2019).
- 23 Jang, S. W. et al. Microscopic understanding of magnetic interactions in bilayer CrI_3 . *Phys Rev Mater* **3**, 031001 (2019).
- 24 Gibertini, M. Magnetism and stability of all primitive stacking patterns in bilayer chromium trihalides. *J Phys D* **54**, 064002 (2020).
- 25 Si, J. S. et al. Revealing the underlying mechanisms of the stacking order and interlayer magnetism of bilayer CrBr_3 . *J Phys Chem C* **125**, 7314-7320 (2021).
- 26 Ren, Y., Ke, S., Lou, W.-K., Chang, K. Quantum phase transitions driven by sliding in bilayer MnBi_2Te_4 . *Phys Rev B* **106**, 235302 (2022).
- 27 Wang, H., Eyert, V., Schwingenschlogl, U. Electronic structure and magnetic ordering of the semiconducting chromium trihalides CrCl_3 , CrBr_3 , and CrI_3 . *J Phys Condens Matter* **23**, 116003 (2011).
- 28 Song, T. et al. Giant tunneling magnetoresistance in spin-filter van der Waals heterostructures. *Science* **360**, 1214-1218 (2018).
- 29 Klein, D. R. et al. Probing magnetism in 2D van der Waals crystalline insulators via electron tunneling. *Science* **360**, 1218-1222 (2018).
- 30 Wang, Z. et al. Very large tunneling magnetoresistance in layered magnetic semiconductor CrI_3 . *Nat Commun* **9**, 2516 (2018).
- 31 Kim, H. H. et al. One million percent tunnel magnetoresistance in a magnetic van der Waals heterostructure. *Nano Lett* **18**, 4885-4890 (2018).
- 32 Ghazaryan, D. et al. Magnon-assisted tunnelling in van der Waals heterostructures based on CrBr_3 . *Nat Electron* **1**, 344-349 (2018).

-
- 33 Jiang, S. et al. Controlling magnetism in 2D CrI₃ by electrostatic doping. *Nat Nanotechnol* **13**, 549-553 (2018).
- 34 Huang, B. et al. Electrical control of 2D magnetism in bilayer CrI₃. *Nat Nanotechnol* **13**, 544-548 (2018).
- 35 Wang, Z. et al. Determining the phase diagram of atomically thin layered antiferromagnet CrCl₃. *Nat Nanotechnol* **14**, 1116-1122 (2019).
- 36 Klein, D. R. et al. Enhancement of interlayer exchange in an ultrathin two-dimensional magnet. *Nat Phys* **15**, 1255-1260 (2019).
- 37 Sun, Z. et al. Giant nonreciprocal second-harmonic generation from antiferromagnetic bilayer CrI₃. *Nature* **572**, 497-501 (2019).
- 38 Kim, M. et al. Micromagnetometry of two-dimensional ferromagnets. *Nat Electron* **2**, 457-463 (2019).
- 39 Kim, H. H. et al. Evolution of interlayer and intralayer magnetism in three atomically thin chromium trihalides. *PNAS* **116**, 11131-11136 (2019).
- 40 Wang, Z. et al. Magnetization dependent tunneling conductance of ferromagnetic barriers. *Nat Commun* **12**, 6659 (2021).
- 41 Song, T. et al. Direct visualization of magnetic domains and moiré magnetism in twisted 2D magnets. *Science* **374**, 1140-1144 (2021).
- 42 Xu, Y. et al. Coexisting ferromagnetic–antiferromagnetic state in twisted bilayer CrI₃. *Nat Nanotechnol* **17**, 143-147 (2022).
- 43 Lado, J. L., Fernández-Rossier, J. On the origin of magnetic anisotropy in two dimensional CrI₃. *2D Materials* **4**, 035002 (2017).
- 44 Bedoya-Pinto, A. et al. Intrinsic 2D-XY ferromagnetism in a van der Waals monolayer. *Science* **374**, 616-620 (2021).
- 45 Chen, W. et al. Direct observation of van der Waals stacking-dependent interlayer magnetism. *Science* **366**, 983-987 (2019).
- 46 Hamer, M. J. et al. Atomic resolution imaging of CrBr₃ using adhesion-enhanced grids. *Nano Lett* **20**, 6582-6589 (2020).
- 47 Han, X. et al. Atomically unveiling an atlas of polytypes in transition-metal trihalides. *J. Am. Chem. Soc.* **145**, 3624-3635 (2023).
- 48 Yin, T. et al. Chiral phonons and giant magneto - optical effect in CrBr₃ 2D magnet. *Adv Mater* **33**, 2101618 (2021).

-
- 49 Kozlenko, D. et al. Spin-induced negative thermal expansion and spin–phonon coupling in van der Waals material CrBr₃. *Npj Comput Mater* **6**, 1-5 (2021).
- 50 Djurdjic-Mijin, S. et al. Lattice dynamics and phase transition in CrI₃ single crystals. *Phys Rev B* **98**, 104307 (2018).
- 51 Ubrig, N. et al. Low-temperature monoclinic layer stacking in atomically thin CrI₃ crystals. *2D Materials* **7**, 015007 (2019).
- 52 Li, T. et al. Pressure-controlled interlayer magnetism in atomically thin CrI₃. *Nat Mater* **18**, 1303-1308 (2019).
- 53 Guo, X. et al. Structural monoclinicity and its coupling to layered magnetism in few-layer CrI₃. *ACS nano* **15**, 10444-10450 (2021).
- 54 Abe, R. Some remarks on perturbation theory and phase transition with an application to anisotropic ising model. *Prog Theor Phys* **44**, 339-347 (1970).
- 55 Krasnow, R., Harbus, F., Liu, L. L., Stanley, H. E. Scaling with respect to a parameter for the gibbs potential and pair correlation function of the S = 1/2 Ising model with lattice anisotropy. *Phys Rev B* **7**, 370 (1973).
- 56 McGuire, M. A., Dixit, H., Cooper, V. R., Sales, B. C. Coupling of crystal structure and magnetism in the layered, ferromagnetic insulator CrI₃. *Chem Mater* **27**, 612-620 (2015).
- 57 Giannozzi, P. et al. QUANTUM ESPRESSO: a modular and open-source software project for quantum simulations of materials. *J Phys Condens Matter* **21**, 395502 (2009).
- 58 Giannozzi, P. et al. Advanced capabilities for materials modelling with quantum ESPRESSO. *J Phys Condens Matter* **29**, 465901 (2017).
- 59 Thonhauser, T. et al. Spin signature of nonlocal correlation binding in metal-organic frameworks. *Phys Rev Lett* **115**, 136402 (2015).
- 60 Lee, K. et al. Higher-accuracy van der Waals density functional. *Phys Rev B* **82**, 081101(R) (2010).
- 61 Hamada, I. van der Waals density functional made accurate. *Phys Rev B* **89**, 121103 (2014).
- 62 Rozzi, C. A. et al. Exact Coulomb cutoff technique for supercell calculations. *Phys Rev B* **73**, 205119 (2006).
- 63 Ismail-Beigi, S. Truncation of periodic image interactions for confined systems. *Phys Rev B* **73**, 233103 (2006).
- 64 Sohler, T., Calandra, M., Mauri, F. Density functional perturbation theory for gated two-dimensional heterostructures: Theoretical developments and application to flexural phonons in graphene. *Phys Rev B*

96, 075448 (2017).

- 65 Garrity, K. F., Bennett, J. W., Rabe, K. M., Vanderbilt, D. Pseudopotentials for high-throughput DFT calculations. *Comp Mater Sci* **81**, 446-452 (2014).
- 66 Dal Corso, A. Pseudopotentials periodic table: From H to Pu. *Comp Mater Sci* **95**, 337-350 (2014).
- 67 Prandini, G. et al. Precision and efficiency in solid-state pseudopotential calculations. *Npj Comput Mater* **4**, 1-13 (2018).
- 68 Pizzi, G. et al. AiiDA: automated interactive infrastructure and database for computational science. *Comp Mater Sci* **111**, 218-230 (2016).
- 69 Huber, S. P. et al. AiiDA 1.0, a scalable computational infrastructure for automated reproducible workflows and data provenance. *Sci Data* **7**, 300 (2020).
- 70 Dumcenco, D., Giannini, E. Growth of van der Waals magnetic semiconductor materials. *J Cryst Growth* **548**, 125799 (2020).
- 71 Zomer, P. J. et al. Fast pick up technique for high quality heterostructures of bilayer graphene and hexagonal boron nitride. *Appl Phys Lett* **105**, 013101 (2014).

Figure captions

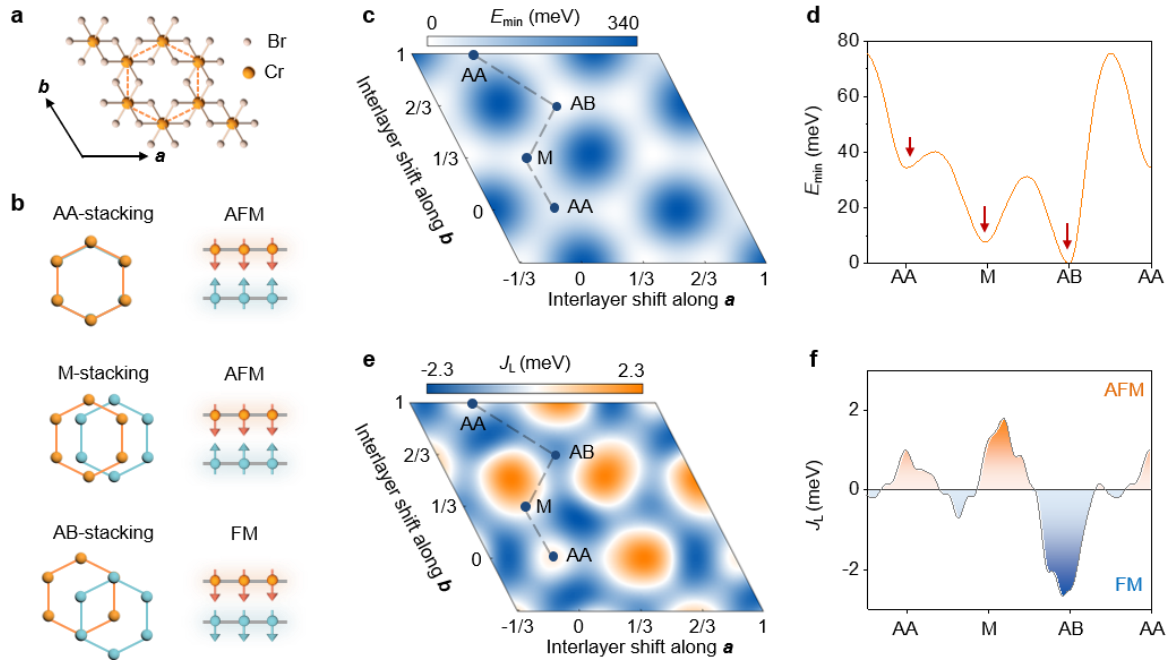


Fig. 1: Total and interlayer exchange energy of bilayer CrBr_3 as predicted by first-principles calculations.

a Top view of monolayer CrBr_3 , where the Cr atoms (orange balls) form a honeycomb lattice and lie inside edge-sharing octahedra formed by the Br atoms (pink balls; \mathbf{a} and \mathbf{b} are the two primitive lattice vectors of the unit cell). **b** Atomic arrangement and interlayer magnetic coupling for the three stacking configurations corresponding to local minima in total energy: AA stacking, where the Cr atoms of the top layer (orange) lie exactly on top of those of the bottom layer (blue); Monoclinic (M) stacking, where the Cr atoms of the top layer are shifted by $[0, 1/3]$ (in units of \mathbf{a} and \mathbf{b}) with respect to the bottom layer; AB stacking, where one of the Cr atoms of the top layer lies above the center of the hexagons in the bottom layer (i.e. with a relative shift by $[1/3, 2/3]$). DFT predicts that AB stacking favors ferromagnetic (FM) interlayer magnetic coupling, while AA and M stackings lead to antiferromagnetic (AFM) ordering. **c** Color plot of the total energy E_{\min} (the minimum energy between FM and AFM configurations, with zero set at the AB FM stacking), as a function of interlayer shift along the two lattice vectors, showing three non-equivalent local minima (indicated by AA, M and AB). **d** Total energy along the grey dashed line in panel c. **e** Color plot of the effective interlayer exchange energy, $J_L = (E_{\text{FM}} - E_{\text{AFM}})/2$, as a function of interlayer shift. The orange regions correspond to AFM ($J_L > 0$) interlayer coupling while the blue regions correspond to FM ($J_L < 0$). **f** The interlayer exchange energy along the grey dashed line path in panel e.

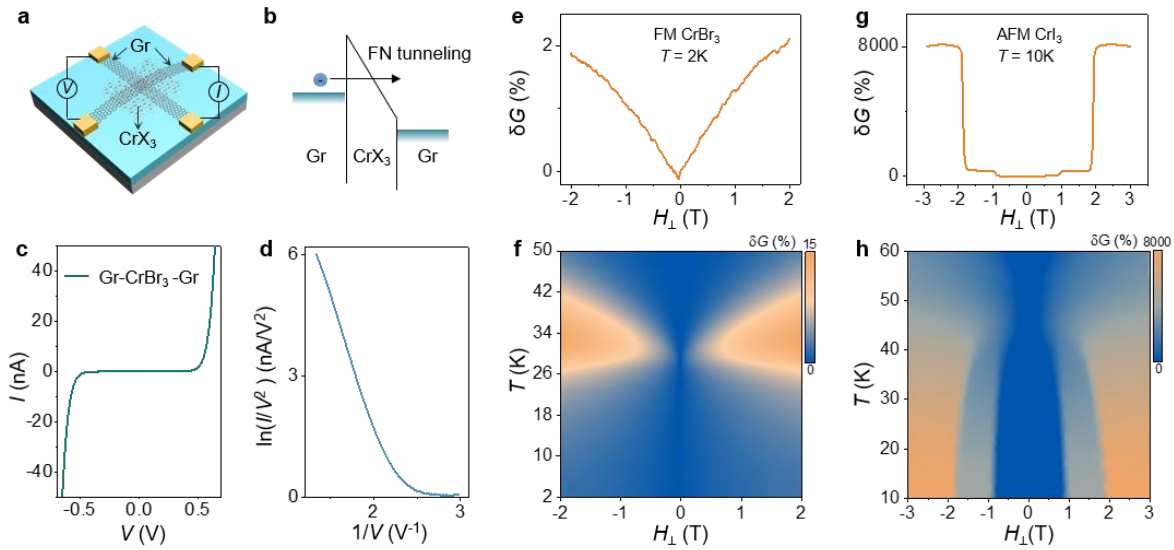


Fig. 2: Probing interlayer magnetic coupling of 2D magnets via tunneling magnetoconductance. **a** Schematics of the tunnel junction devices, where electrons tunnel between two graphite sheets (Gr) separated by a magnetic CrX_3 tunnel barrier. **b** Schematic energy diagram of the tunnel junctions illustrating the Fowler-Nordheim (FN) tunneling regime, with the electric field generated by the applied bias (V) that tilts the conduction band, causing the tunneling probability to increase exponentially. **c** Low-temperature ($T = 2$ K) tunneling current (I) across a four-layer CrBr_3 tunnel barrier as a function of applied voltage with $\ln(I/V^2)$ scaling linearly with $1/V$ for sufficiently large bias, as shown in **d**. **(e)** $\delta G(H, 2\text{K})$ measured across the four-layer ferromagnetic CrBr_3 tunnel barrier ($V = 0.6$ V), exhibiting only a small change (2%) as a function of magnetic field. **f** Color plot of the magnetoconductance $\delta G(H, T)$, showing the “lobes” around T_C characteristic of ferromagnetic barriers. **g** $\delta G(H, 10\text{K})$ measured across an antiferromagnet CrI_3 tunnel barrier (~ 7 nm, $V = 0.5$ V), showing two characteristic spin-flip transition fields (jumps) at 0.9T and twice this value 1.8T. **h** Color plot of $\delta G(H, T)$ for the same CrI_3 tunnel barrier, showing the evolution of the spin-flip transition fields with temperature (in all measurements shown in this figure, the magnetic field is applied perpendicular to the a - b plane of CrX_3).

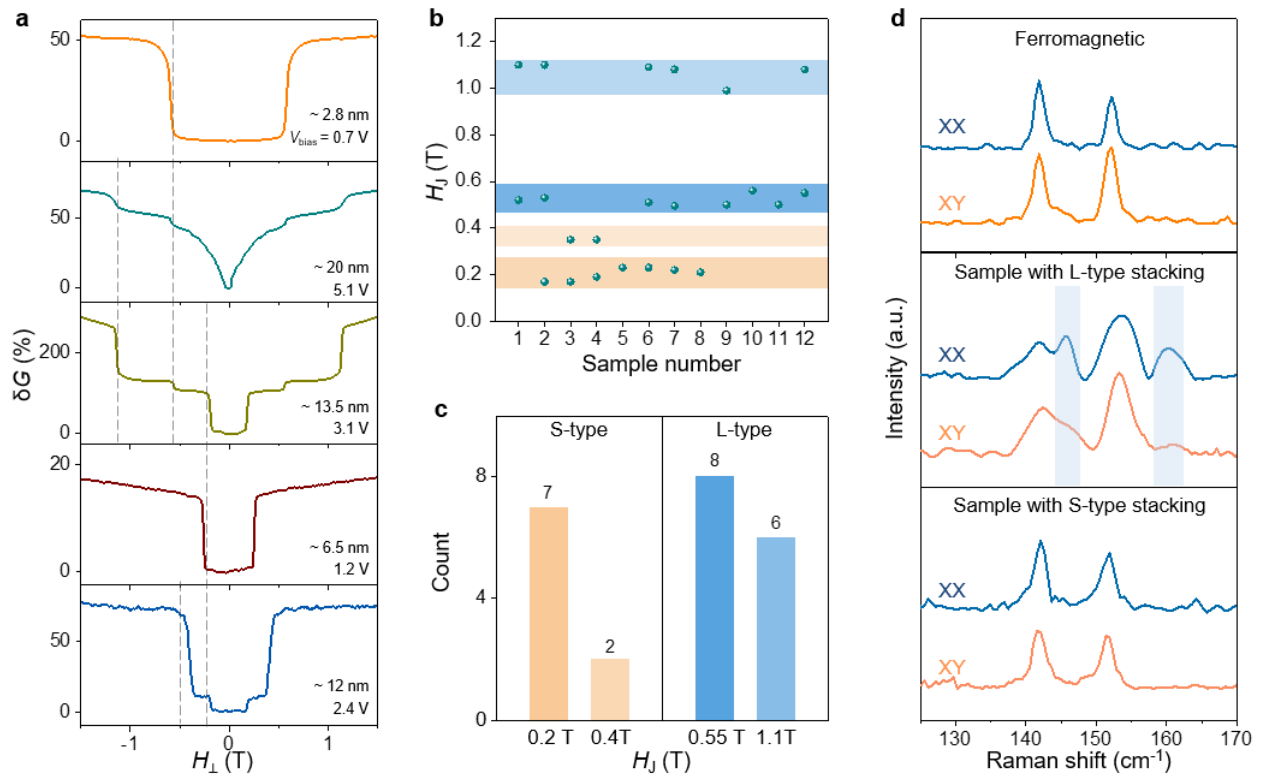


Fig. 3: Identification of CrBr₃ multilayers with different stacking order. **a** Low-temperature tunneling magnetoconductance $\delta G(H)$ of five representative CrBr₃ multilayers, showing jumps in at several transition fields (H_J ; indicated by the vertical grey dashed lines). **b** Summary of the different values of H_J measured in twelve CrBr₃ multilayers (the $\delta G(H)$ and thickness of each sample can be found in Supplementary Fig. 2). The values can be classified into two groups: 0.55 T and twice this value 1.1 T (blue rectangles), and 0.2 T and twice this value 0.4 T (orange rectangles). **c** Histogram of transition field distribution, as extracted from all devices measured. **d** Raman spectra of CrBr₃ multilayers with ferromagnetic interlayer coupling (top panel), antiferromagnetic L-type stacking (middle panel) and antiferromagnetic S-type stacking (bottom panel), measured under both parallel (XX, blue lines) and crossed (XY, orange lines) polarization configurations at 10 K. The spectrum of the CrBr₃ layer with antiferromagnetic L-type stacking exhibits two additional peaks (indicated by the blue rectangles in the middle panel) compared to that of the multilayers with antiferromagnetic S-type stacking and ferromagnetic interlayer coupling, whose intensity varies in different polarized configurations, reflecting the lower symmetry of L-stacking.

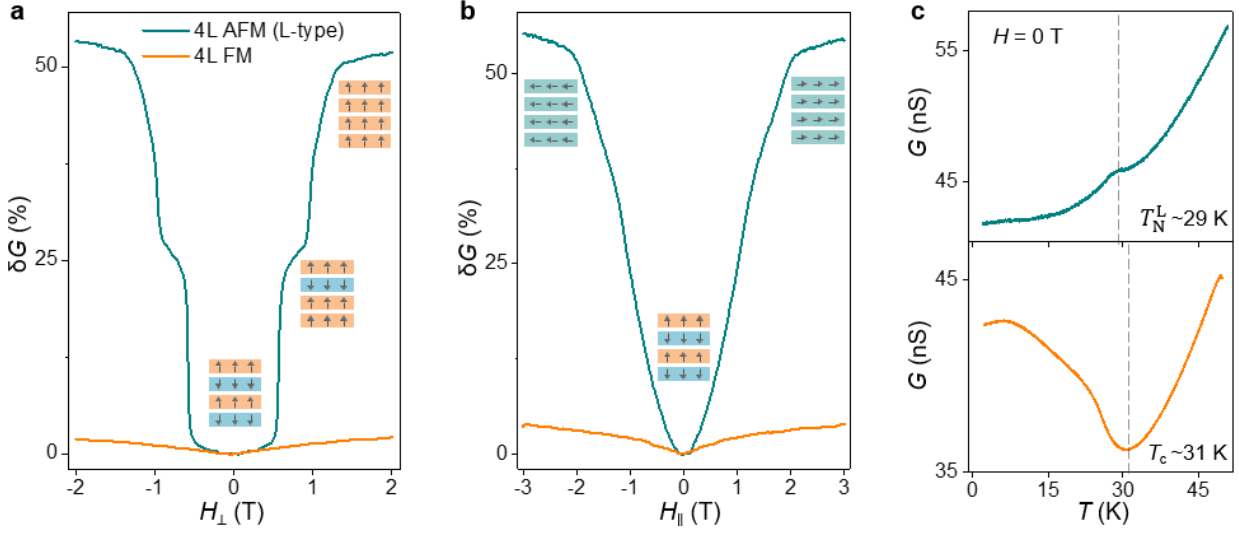


Fig. 4: Comparison of transport through four-layer CrBr₃ tunnel barriers with either ferromagnetic or L-type antiferromagnetic interlayer coupling. **a** Out-of-plane (H_{\perp}) and **b** in-plane (H_{\parallel}) magnetic field dependence of the tunneling magnetoconductance ($\delta G(H, 2K) = (G(H, T) - G_0(2K)) / G_0(2K)$) measured on the four-layer CrBr₃ tunnel barriers with either L-type antiferromagnetic (green line) or ferromagnetic (orange line) interlayer coupling. **c** Temperature dependence of the tunneling conductance (top panel: antiferromagnetic L-type stacking; bottom panel: ferromagnetic interlayer coupling) at zero magnetic field. The measurements allow the determination of the Néel temperature ($T_N^L \sim 29$ K; top panel) and Curie temperature ($T_C \sim 31$ K; bottom panel), marked by the vertical dashed lines. In this and later figures, the bias voltage is 0.6 V and 0.7 V for the 4L ferromagnetic and the L-type antiferromagnetic device, respectively.

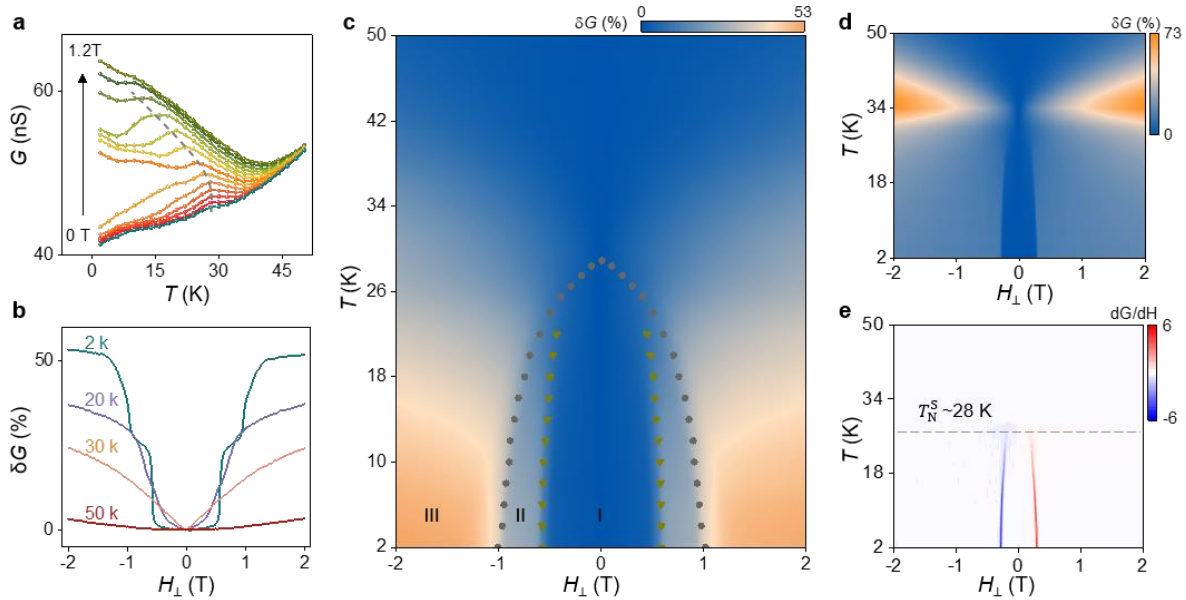




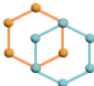
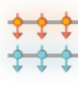


Fig. 5: Temperature dependent magnetotransport response of L-type and S-type antiferromagnetic CrBr_3 barriers. **a** Temperature dependence of the tunneling conductance of a L-type antiferromagnetic four-layer CrBr_3 barrier measured at different out-of-plane magnetic fields. The kink in each curve (traced by the grey dashed line) follows the evolution of the onset of magnetic order with applied field. **b** Tunneling magnetoconductance plotted as a function of H for selected values of T : as T increases, $\delta G(H, T)$ decreases and the jumps shift to lower values of H . **c** Color plot of $\delta G(H, T)$, showing the phase diagram of four-layer antiferromagnetic L-type stacked CrBr_3 . The circles and triangles are extracted either from the G -vs- T curves (see panel a) or from fields at which the magnetoconductance jumps occur (see panel b). **d** Color plots of $\delta G(H, T)$ and **e** $dG/dH(H, T)$ measured across on CrBr_3 multilayer tunnel barrier (~ 6.5 nm, $V = 1.2\text{V}$) comprising layers with both ferromagnetic and S-type antiferromagnetic stacking (accounting for the concomitant presence of the characteristic magnetic lobes near the ferromagnetic T_C and the jump characteristic of antiferromagnetic interlayer coupling). Tracking the temperature at which the magnetoconductance jumps disappear, we estimate the transition temperature for S-type antiferromagnets to be $T_N^S \sim 28$ K.

Table 1 Summary of CrBr ₃ with different magnetic states				
Stacking type	Interlayer magnetic order	Symmetry information	Estimated critical temperature	Magnetoconductance jumps
AA-stacking 	S-type AFM 	$R\bar{3}$	~ 28 K	~ 0.2 T and 0.4 T
M-stacking 	L-type AFM 	$C2/m$	~ 29 K	~ 0.55 T and 1.1 T
AB-stacking 	FM 	$R\bar{3}$	~ 31 K	No jumps